Author Manuscript

Author Manuscript

Author Manuscript

Author Manuscript

HHS Public Access

Author manuscript

Soft Matter. Author manuscript; available in PMC 2025 January 17.

Published in final edited form as:

Soft Matter. ; 20(3): 693–703. doi:10.1039/d3sm01332d.

Deciphering the Influence of Y12L and N17H Substitutions on the Conformation and Oligomerization of Human Calcitonin

Jiajia Yan[1,2], **Ying Wang**[1], **Xinjie Fan**[1], **Yu Zou**[3], **Feng Ding**[4,*], **Fengjuan Huang**[2,*], **Yunxiang Sun**[1,4,*]

[1]School of Physical Science and Technology, Ningbo University, Ningbo 315211, China

[2]Ningbo Institute of Innovation for Combined Medicine and Engineering (NIIME), Ningbo Medical Center Lihuili Hospital, Ningbo 315211, China

[3]Department of Sport and Exercise Science, Zhejiang University, Hangzhou 310058, China

[4]Department of Physics and Astronomy, Clemson University, Clemson, SC 29634, United States

Abstract

The abnormal aggregation of human calcitonin (hCT) hormone peptides impairs their physiological function, leading to harmful immune responses and cytotoxicity, which limits their clinical utility. Interestingly, a representative hCT analog incorporating Y12L and N17H substitutions (DM-hCT) has shown reduced aggregation tendencies while maintaining bioactivity. But the molecular mechanism of Y12L and N17H substitutions on the conformational dynamics of hCT remains unclear. Here, we systematically investigated the folding and self-assembly dynamics of hCT and DM-hCT using atomistic discrete molecular dynamics (DMD) simulations. Our findings revealed that hCT monomers predominantly adopted unstructured conformations with dynamic helices. Oligomerization of hCT resulted in the formation of β-sheet-rich aggregates and β-barrel intermediates. The Y12L and N17H substitutions enhanced helical conformations and suppressed β-sheet formation in both monomers and oligomers. These substitutions stabilized the dynamic helices and disrupted aromatic interactions responsible for β-sheet formation at residue 12. Notably, DM-hCT assemblies still exhibited β-sheets in phenylalanine-rich and C-terminal hydrophobic regions, suggesting that future optimizations should focus on these areas. Our simulations provide insights into the molecular mechanisms underlying hCT aggregation and the amyloid-resistant effects of Y12L and N17H substitutions. These findings have valuable implications for the development of clinical hCT analogs.

* fding@clemson.edu, hfj_1130@163.com, sunyunxiang@nbu.edu.cn.

Author contributions

Y. S., F. D., and F. H. conceived and designed the project; J. Y., X. F., Y. W. and Y. Z. performed the simulations and analyzed data; Y. S., F. H., and F. D. wrote the paper, and all authors approved the manuscript.

Supporting Information

The Supporting Information is available free of charge at …..

The initial structures of hCT and DM-hCT monomers (Fig. S1); equilibrium and convergence assessments of hCT and DM-hCT monomer simulations (Figs. S2&S3); equilibrium and convergence assessments for simulations of four hCT and four DM-hCT peptides (Figs. S4&S5).

Declaration of competing interest

There are no conflicts of interest to declare.

Author Manuscript Author Manuscript Author Manuscript Author Manuscript

Graphical Abstract

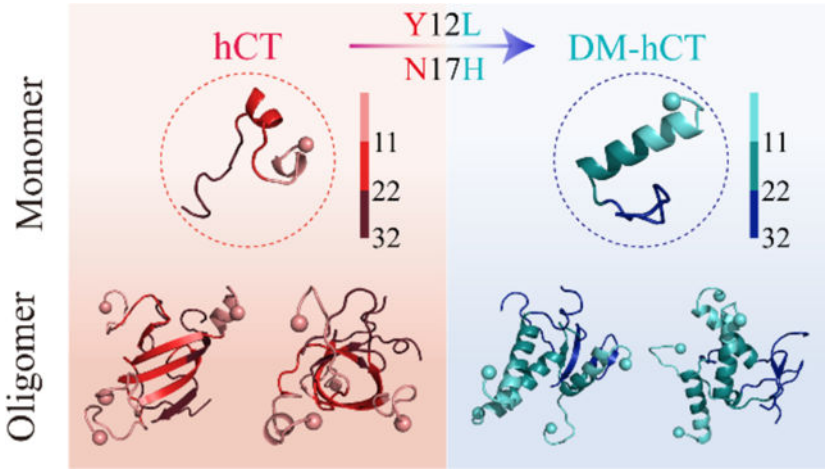

Human calcitonin monomers displayed dynamic helical structures and readily aggregated into β-sheet-rich oligomers, including β-barrel intermediates. The Y12L and N17H substitutions in human calcitonin enhanced helical conformations and partially inhibited the formation of β-sheet-rich oligomers.

Keywords

Amyloid aggregation; Human calcitonin; Discrete molecular dynamics

1. Introduction

Human calcitonin (hCT) is a 32-amino acid polypeptide hormone secreted by the C-cells of the thyroid gland, playing a crucial role in regulating calcium-phosphorus metabolism within the body[1]. The central physiological function of hCT revolves around its interaction with the skeletal system to maintain calcium homeostasis within the human body[2]. This is primarily achieved by preserving bone mass through inhibiting osteoclasts, a specific type of bone-associated cell responsible for bone resorption[3]. The capability of hCT to suppress bone resorption has led to its application in treating conditions like osteoporosis, hypercalcemia, and Paget's disease for over two decades[4, 5]. However, due to its significant aggregation tendency and resulting reduced bioactivity, the clinical use of hCT has been discontinued, as recognized by the FDA[6]. Furthermore, amyloid deposits of hCT have been detected in patients with medullary thyroid carcinoma (MTC), implying a potential link between MTC and hCT aggregation[7, 8]. The irreversible aggregation of peptides leading to amyloid deposits in human tissues and organs is recognized to be associated with various amyloid diseases, including Alzheimer's disease (AD) with amyloid-β (Aβ) and tau, and type 2 diabetes (T2D) with human islet amyloid polypeptide (hIAPP). Similar to peptides associated with amyloid diseases (such as Aβ, tau, and hIAPP), prior research has shown that the aggregation of hCT notably reduced the viability of SH-SY5Y cells *in vivo*[9]. Therefore, the abnormal accumulation of hCT compromises its reliability as a pharmaceutical agent in clinical applications.

Author Manuscript Author Manuscript Author Manuscript Author Manuscript

The anomalous aggregation of the hCT peptide drug leads to a marked reduction in bioactivity[5], undesirable immune responses[10], and drug-induced cytotoxicity[9]. Salmon calcitonin (sCT), known for its considerably reduced aggregation tendency compared to hCT, serves as a clinical alternative[11]. Despite sCT's notably weaker potency in comparison to hCT[12], its administration necessitates frequent injections due to its relatively short half-life of only 1 hour[13]. Furthermore, sCT administration triggers immunogenic reactions (e.g., anorexia and vomiting) owing to its sequence similarity with hCT at approximately 50%[1, 14]. Therefore, the concept of crafting non-amyloidogenic analogues of hCT, closely mirroring its physicochemical properties and sequence, emerges as an ideal strategy to surmount these challenges[11, 12]. Mitigating hCT amyloidosis by strategically replacing specific amyloidogenic residues is particularly intriguing[9, 12, 15, 16], given the anticipated advantages of high biocompatibility, limited immunogenicity, and the potential to retain hCT's functionality. Consequently, hCT analogues with diminished aggregation propensity hold promise for clinical applications as therapeutic interventions against bone-related conditions.

Understanding the molecular mechanisms by which hCT monomers assemble into fibrils is crucial for developing fibrillation-resistant hCT analogs. The fibrillation process of hCT follows a typical nucleation-dependent sigmoidal kinetics. Isolated hCT monomers kickstart β-sheet-rich protofibril formation, transitioning from helical accumulation to sequential conformational changes, ultimately resulting in mature fibril growth[13, 15, 17, 18]. hCT monomer exhibited dynamic helical conformations *in vivo*[12, 19] and *in silico*[20, 21]. The nucleation of hCT triggers a shift from helix to β-sheet around residue G10 and a transition from random coil to β-sheet for residues F22, A26, and A31[15]. The hCT segment ^{15}DFNKF[19] readily formed fibrils, highlighting its pivotal role in hCT aggregation[17, 22]. Nitration of the Y12[9] or phosphorylation of the T13[18] in hCT can hinder aggregation, underscoring their significance in this aggregation-prone region. The hCT analogue with F16L and F19L substitutions exhibited slower aggregation than the wild type but faster than the TL-hCT with Y12L, F16L, and F19L substitutions[15]. The phCT, with five residues replaced by their corresponding sCT counterparts - Y12L, N17H, A26N, I27T, and A31T - demonstrated low aggregation propensity and maintained a solution structure similar to sCT[12]. Our recent simulation study uncovered that the aromatic residues (Y12, F16, F19, and F22) and the hydrophobic residues at the C-terminal (A26, I27, V29, and A31) are key drivers in the formation of β-sheet structures during hCT aggregation[20]. Another hCT analog with Y12L and N17H double mutations (DM-hCT) can inhibit hCT aggregation without altering its bioactivity of binding to the hCT receptor[16, 23]. Furthermore, the presence of DM-hCT can also inhibit the fibrillization of wild-type hCT[16]. With just two residue substitutions and a physiological function similar to hCT, DM-hCT could potentially provide a valuable therapeutic alternative to hCT. However, the impact of Y12L and N17H substitutions on the conformational dynamics of hCT remains uncertain, which is crucial for the clinical utilization of DM-hCT and the development of other amyloid-resistant hCT analogs.

To explore the impact of Y12L and N17H double substitutions on the conformational dynamics of hCT monomers and aggregates, we employed atomistic discrete molecular dynamics (DMD) simulations with the Medusa force field[24, 25] to conduct both one-

Author Manuscript Author Manuscript Author Manuscript Author Manuscript

and four-peptide simulations of hCT and DM-hCT. Our extensive long-timescale DMD simulations revealed that hCT monomers primarily adopted unstructured conformations, with dynamic helices occurring around residues 4–21. The Y12L and N17H substitutions increased the stability of the dynamic helix around residues 4–21 and inhibited the transition towards transient β-sheet conformations of residues 8–12 in hCT monomers. The oligomerization of hCT resulted in the formation of β-sheet-rich aggregates and β-barrel intermediates. Formation of β-sheets within the hCT aggregates included residues 8–31, with a prominent presence around the phenylalanine-rich region of residues 16–25. Compared to the hCT oligomers, self-assemblies of DM-hCT exhibited an enhancement of helix conformations around residues 4–21 and an inhibition of β-sheet formations around residues 8–14. The phenylalanine-rich region and C-terminal hydrophobic tail still displayed inter-peptide β-sheets in DM-hCT aggregates. Future improvements to enhance DM-hCT's amyloid-resistance should focus on minimizing mutations to effectively reduce the remaining β-sheets. In conclusion, our simulations suggest that the experimentally determined amyloid-resistant Y12L and N17H substitutions[16, 23] are achieved by stabilizing the dynamic helical conformation and suppressing its conversion to β-sheet structures. Our findings not only elucidate the molecular mechanism behind hCT aggregation and the amyloid-resistant effects of Y12L and N17H double substitutions but also offer valuable insights for developing next-generation hCT analogs for clinical applications.

2. Materials and methods

2.1 Molecular Systems.

The experimentally determined structures of hCT and DM-hCT remain unclear. To initiate our simulations, we utilized the NMR-characterized phCT monomer structure[12] (PDB ID: 2jxz) as a template, using PyMol mutagenesis to construct the initial conformations of hCT and DM-hCT monomers. The primary amino acid sequences and structures of hCT and DM-hCT are outlined in Table 1 and Fig. S1. For each peptide type, we conducted two molecular systems involving one and four peptides to explore monomer conformation and self-assembly dynamics. Within each system, we executed fifty independents atomistic DMD simulations, commencing from distinct initial states encompassing coordinates, orientations, and velocities. In simulations involving multiple peptides, four peptides were randomly situated (with both positions and orientations) within a 9.5 nm cubic simulation box, maintaining a minimum intermolecular distance of 1.5 nm. To prevent bias from initial states and ensure comprehensive conformational sampling, each independent simulation, whether with one or four peptides, extended up to 1000 ns. Further details about each molecular system are consolidated in Table 2.

2.2 Discrete Molecular Dynamics (DMD) Simulations.

All simulations were conducted at a temperature of 300K using the atomistic discrete molecular dynamics (DMD) algorithm coupled with the Medusa force field[26, 27]. The Medusa force field has been extensively validated for its accuracy in predicting changes in protein stability and protein-ligand binding affinity upon mutation[28, 29], making it well-suited for this study. DMD is a rapid and predictive molecular dynamics algorithm that employs discrete step-wise functions to model the continuous potential functions used in

Author Manuscript Author Manuscript Author Manuscript Author Manuscript

classic molecular dynamics (MD)[25, 30]. Similar to traditional MD force fields, the Medusa force field considers both bonded interactions (such as covalent bonds, bond angles, and dihedrals) and nonbonded interactions (including van der Waals, solvation, hydrogen bond, and electrostatic terms). Solvation energy was computed using the effective energy function proposed by Lazaridis and Karplus[31]. Hydrogen bonds were explicitly modeled using a reaction-like algorithm[24]. Electrostatic interactions between charged atoms were computed using the Debye-Hückel approximation with a Debye length of approximately 10 Å under physiological conditions. The DMD software is available to academic researchers through Molecules In Action, LLC (www.moleculesinaction.com). In our simulations, the units of mass, time, length, and energy were set to 1 Da, approximately 50 fs, 1 Å, and 1 kcal/mol, respectively.

The predictive capabilities of DMD simulations using the Medusa force field and the EEF1 implicit solvation model have been validated in previous research[25, 26]. This validation includes accurately modeling native states with both secondary and tertiary structures in *ab* initio protein folding simulations[24, 25] and consistently reproducing computationally derived conformational ensembles that match single-molecule FRET measurements in the conformational dynamics of multi-domain proteins[32, 33]. Additionally, the accuracy of the Medusa force field, in combination with the EEF1 implicit solvation model, has been benchmarked against standard MD simulations that utilize an explicit solvent model with various force fields such as GROMOS96, OPLS-AA, AMBER99SB-ILDN, and CHARMM36m in our earlier studies[34, 35]. Our recent research successfully replicated the experimentally examined self-assembly of hCT into β-sheet-rich structures and amyloid-resistant mutants of TL-hCT and phCT[20]. These findings highlight the Medusa force field's capability to faithfully represent the conformational dynamics of hCT and its analogs.

2.3 Analysis Methods.

We employed the dictionary of secondary structures of proteins (DSSP) method for the analysis of secondary structures[36]. Residue-pairwise contact occurrence was defined when the minimum distance between heavy atoms of two nonconsecutive residues was less than 0.55 nm[37]. Hydrogen bonding was identified if the distance between backbone N and O atoms was ≤ 3.5 Å, and the N–H•••O angle was ≥ 120°[38]. Cluster analysis utilized the Daura algorithm with a backbone atom deviation cutoff of 0.35 nm[39]. Two-dimensional (2D) free energy (also known as potential mean force, PMF) surfaces were constructed using the formula −RT ln P(x, y), where P(x, y) represents the probability of a conformation having specific parameter values of x and y[40]. An oligomer was identified as a β-barrel if its β-strand segments formed a closed cycle with each β-strand connected by at least two hydrogen bonds to neighboring β-strands[35, 41].

Author Manuscript Author Manuscript Author Manuscript Author Manuscript

3. Results and Discussion.

3.1 The Y12L and N17H substitutions of hCT increased the stability of dynamic helical conformations and inhibited the formation of transient β-hairpin structures in the monomers.

Fifty independent microsecond-scale simulations were conducted to thoroughly explore the monomeric conformational dynamics of hCT and DM-hCT, ensuring comprehensive sampling. The efficiency of conformational sampling and equilibrium were evaluated through structural parameters such as radius of gyration (Rg), number of backbone hydrogen bonds and heavy atom contacts, and secondary structure content over simulation time (Figs. S2 and S3). Pronounced fluctuations without consistent trends confirmed that our extended DMD simulations were not trapped and sufficient sampling was attained. The ensemble-averaged time evolution of these parameters across fifty independent simulations demonstrated minimal changes in the last 500 ns, indicating reasonable equilibration of both molecular systems.

For each molecular system, one trajectory was randomly selected from the fifty independent DMD simulations to illustrate the conformational dynamics of each peptide by monitoring the time evolution of the secondary structure of each residue (Fig. 1a&b). The conformations of both hCT and DM-hCT monomers displayed notable dynamics, undergoing frequent conformational changes. The N-terminal and central regions (residues 4–21) formed dynamic helical structures, whereas the C-terminal residues occasionally exhibited transient β-sheets.

The secondary structure was further analyzed using the last 500 ns of simulation data from fifty independent trajectories (Fig. 1c&d). The average secondary structure content indicated that both hCT and DM-hCT monomers predominantly adopted unstructured conformations (including random coil and bend structures) with propensities of ~68.6% and ~64.6%, respectively (Fig. 1c&d). The helical population of hCT (~15.3%) was smaller than that of DM-hCT (~19.8%), suggesting that Y12L and N17H substitutions enhanced helical conformations. Previous CD spectroscopy assays on hCT and DM-hCT indicated that DM-hCT exhibited a higher helical content than hCT[16], consistent with our simulation results. The average helical propensity for each residue of hCT exhibited two helical regions around residues 4–12 and 14–21, with the latter (~50%) showing a stronger tendency than the former (~25%) (Fig. 1d). Previous solid-state NMR studies revealed similar helical regions[15, 42, 43.] For instance, high-resolution NMR spectroscopy demonstrated local helical structures around residues 10 and 13–21, while F22, A26, and A31 exhibited random coil structures in hCT monomers[15]. The average helical tendencies in both regions (residues 4–12 and 14–21) were enhanced in DM-hCT. Additionally, a weak enhancement of helix formation around residue 12 was observed in DM-hCT, which was relatively weak in the hCT monomer.

In comparison to the helical structure, the average β-sheet content in hCT and DM-hCT was relatively low, with a propensity of approximately 4.4% and 4.1%, respectively (Fig. 1c). This observation aligns with the analysis of the time-evolution secondary structure dynamics of each residue, where β-sheet conformations were highly transient and frequently

Author Manuscript Author Manuscript Author Manuscript Author Manuscript

converted into random coil and bend structures (Fig. 1a&b). The top four most populated conformational clusters of hCT and DM-hCT, which accounted for 8.1% and 10.5% of the conformations, respectively, further confirmed that both types of peptides primarily adopted unstructured conformations with partial helices, and DM-hCT exhibited a higher helical tendency (Fig. 1e&f).

3.2 The double mutants Y12L and N17H enhanced the helical conformation while suppressing the transition towards transient β-hairpin structures of the hCT monomer.

Residue-pairwise contact frequencies within hCT and DM-hCT monomers were further analyzed to investigate the effects of the Y12L and N17H substitutions on the conformation of the hCT monomer (Fig. 2). Consistent with prior NMR experiments[15, 42, 43] and secondary structure analysis (Fig. 1d), the hCT monomer exhibited two helical patterns along the diagonal around residues 4–12 and 14–21 (contact patterns and conformations 1 & 2 in Fig. 2a&b). An obvious β-hairpin contact pattern, oriented perpendicular to the diagonal, was observed, involving β-strands formed by residues 18–22 and 26–30 (contact patterns and conformations 3 in Fig. 2a&b). Additionally, two relatively weak β-sheet patterns were also observed, involving the formation of β-strands around residues 8–12 vs. 19–23 and residues 9–13 vs. 27–31 (contact patterns and conformations 4 & 5 in Fig. 2a&b). These β-sheets were primarily stabilized by interactions among hydrophobic residues.

The DM-hCT displayed a continuous helical contact pattern around residues 4–21 (contact patterns and conformations 1 & 2 in Fig. 2c&e), encompassing both helical regions found in hCT (i.e., residues 4–12 and 14–21). Analysis of the differences in residue-pairwise contact frequency between DM-hCT and hCT monomers revealed that the double mutations Y12L and N17H did not alter the helical region but enhanced the stability of the helical conformations (i.e., contact pattern regions 1 & 2 in Fig. 2d). For instance, the propensities of the helical contact patterns around residues 4–12 and 14–21 were greater than those of hCT. This observation can be explained by the inherent φ and ψ preferences of amino acids[44, 45]. For example, tyrosine favored β-sheet conformations over helices, whereas leucine exhibited a preference for helical structures over β-sheets[44, 45]. Additionally, histidine had a slightly stronger inclination towards helical conformations compared to asparagine[44, 45]. The transient β-sheets involving residues 8–12 vs. 19–23 and residues 9–13 vs. 26–31 (contact patterns and conformations 4 & 5 in Fig. 2c–e) were suppressed. This suppression can be attributed to the Y12L and N17H mutations enhancing the helical stability around residues 4–21. As a result, there was a slightly stronger interaction between residues 15–19 and 27–31 to balance the exposed surface areas of C-terminal hydrophobic residues (contact pattern and conformation 3 in Fig. 2c–e). This explained why the Y12L and N17H substitutions only inhibited β-sheet formation around the residue 12 region, without affecting the central aromatic regions in the β-sheet propensity of each residue (Fig. 1d). The enhanced stability of the dynamic helix in DM-hCT compared to hCT was consistent with the CD measurements[16, 23]. Overall, our analysis of residue-pairwise contacts indicated that the Y12L and N17H mutations stabilize the dynamic helical conformations, thus contributing to the suppression of the conformational transition from helix to β-sheet in the hCT monomer.

Author Manuscript Author Manuscript Author Manuscript Author Manuscript

3.3 The double mutants Y12L and N17H inhibited the formation of inter-peptide contacts and hydrogen bonds while enhancing intra-peptide contacts and hydrogen bonds.

To investigate the effects of the Y12L and N17H substitutions on the self-assembly of hCT, we conducted fifty independent four-peptide simulations, each with a duration of up to 1000 ns. The time evolution of the radius of gyration, total number of contacts and hydrogen bonds, as well as the average secondary structure contents, all indicated that our molecular systems reached steady states of oligomerization during the last 500 ns (Figs. S4 and S5). Therefore, we utilized the simulation data from the final 500 ns of each independent DMD trajectory for the equilibrium analysis of aggregate structures and conformational dynamics. The analysis of self-assembly dynamics, as monitored through the time evolution of inter- and intra-peptide contacts and hydrogen bonds, revealed that both hCT and DM-hCT readily formed oligomers, but they exhibited distinct conformational characteristics in these parameters (Fig. 3a&b). Therefore, we further computed the probability distribution functions for both inter- and intra-peptide contacts and hydrogen bonds within the self-assemblies of both peptides, utilizing the last 500 ns of simulation data from all fifty independent trajectories (Fig. 3c). Consistent with the findings from the self-assembly dynamics analysis (Fig. 3a&b), the conformations of hCT oligomers displayed a greater number of inter-peptide contacts and hydrogen bonds compared to DM-hCT aggregates (Fig. 3c). Conversely, DM-hCT assemblies exhibited a higher count of intra-peptide contacts and hydrogen bonds than hCT aggregates.

3.4 The double substitutions Y12L and N17H in hCT resulted in self-assemblies with more helical and less β-sheet conformations.

The average secondary structure was analyzed to uncover the effects of Y12L and N17H substitutions on the structure of hCT aggregates. Oligomerization of hCT resulted in a noticeable enhancement of β-sheet content and a decrease in helix content. For example, the averaged β-sheet and helix contents of hCT aggregates were approximately 18.3% and 10.6%, respectively (Fig. 4a), while hCT monomers exhibited approximately 4.4% β-sheet and 15.3% helix content (Fig. 2c). The substitutions of Y12L and N17H in hCT led to DM-hCT having a significantly higher helix content and lower β-sheet and unstructured conformations compared to hCT (Fig. 4a). The average secondary structure propensity of each residue from hCT and DM-hCT aggregates suggested that the double mutations of Y12L and N17H enhanced the helical conformations around residues 4–21 and inhibited the unstructured conformations of residues 4–19, as compared to hCT oligomers (Fig. 4b). Additionally, the inhibition of β-sheet formation was predominantly observed around residues 8–12, with a relatively milder suppression effect observed around residues 20–22.

The average helix and β-sheet ratios from each independent oligomerization simulation for hCT and DM-hCT during the last 500 ns revealed distinct conformational preferences. DM-hCT aggregates showed a higher propensity for helical structures, while hCT aggregates exhibited a higher occurrence of β-sheet conformations (Fig. 4c). To delve deeper, we calculated the conformational potential mean force (PMF), often referred to as the free energy landscape, as a function of the helix and β-sheet ratios (Fig. 4d). Both systems exhibited broad energy basins but in different regions. The most favorable conformations for hCT oligomers were characterized by a helix content of 0%~12% and a β-sheet

Author Manuscript Author Manuscript Author Manuscript Author Manuscript

population of 7%~22% on the PMF surface. In contrast, the Y12L and N17H substitutions shifted the preference towards conformations with a higher helix content and a lower β-sheet population. This evident shift towards more helices and fewer β-sheets in DM-hCT compared to hCT suggested that the double substitutions of Y12L and N17H suppressed hCT fibrillization *in vivo*[16, 23] by enhancing helix formation and preventing β-sheet structures.

3.5 The double substitutions Y12L and N17H prevented inter-peptide interactions around residues 8–12 from forming β-sheet conformations.

To explore the critical interactions responsible for the aggregation of hCT and elucidate the amyloid-resistant mechanism arising from the double mutants Y12L and N17H, we computed the probabilities of intra- and inter-chain contacts between all pairs of residues, considering both main-chain and side-chain atoms (Fig. 5). Intra-peptide residue-pairwise contact frequencies within hCT self-assemblies primarily revealed two helical regions (residues 4–12 and 14–21) and one β-hairpin structure (residues 19–31) as dominant contact patterns (Fig. 5a&b). Examination of inter-residue interactions involving side-chain atoms indicated that the stability of the β-hairpin structure was mainly driven by hydrophobic interactions between residue F19 and the C-terminal hydrophobic tail. Furthermore, multiple inter-peptide β-sheet contact patterns, perpendicular to the diagonal, encompassed residues 8–31 and were primarily governed by interactions between aromatic (e.g., Y12, F16, F19, H20, and F22) and hydrophobic (L9, F16, F19, F22, A26, I27, V29, and A31) residues in hCT oligomers (Fig. 5a&b). This finding highlighted the critical role of hydrophobic and aromatic residues in mediating inter-peptide β-sheet formation during hCT self-assembly, which aligns with previous studies on hCT and amyloid-resistant analogs aggregation[9, 15, 17, 20, 22]. For instance, prior NMR measurements conclusively established that interactions between the central aromatic residues and the C-terminal hydrophobic residues were the primary driving forces behind the nucleation and fibril elongation of hCT[15, 46]. Substitutions such as Y12L, F16L, and F19L resulted in relatively weak amyloid aggregation, as exemplified in TL-hCT[15]. Another polar hCT analog, phCT, was characterized by five residue replacements (Y12L, N17H, A26N, I27T, and A31T) and exhibited a low propensity for aggregation[12]. Our results are in alignment with these previous studies[9, 12, 20], which highlighted the significance of aromatic and hydrophobic residues (L9, Y12, F16, F19, H20, F22, A26, I27, V29, and A31) in the nucleation and fibril elongation of hCT.

The analysis of residue-pairwise contacts in DM-hCT self-assemblies, compared to hCT oligomers, indicated that the Y12L and N17H substitutions led to an enhancement of helical conformations around residues 4–21 (Fig. 5c–e). The Y12L substitution disrupted the formation of inter-peptide β-sheets, which were primarily driven by the interaction of the aromatic residue Y12 with F16, F19, H20, and F22 in hCT aggregates. Additionally, enhancement of helical formation in residues 4–21 also suppressed their participation with the C-terminal hydrophobic tail in β-sheet structures. Due to the intrinsic biophysical property of the aromatic phenylalanine favored β-sheet formation over α-helix[44, 45], phenylalanine residues were commonly found around the β-sheet core in many amyloid peptides, such as the segments KLVFFAE in Aβ[47, 48] and NFGAIL in hIAPP[49, 50]. The

Author Manuscript Author Manuscript Author Manuscript Author Manuscript

segments ^{16}FHKFHTF^{22} and ^{26}AIGVGA^{31} in DM-hCT aggregates remained populated with inter-peptide β-sheet structures because there were no alterations in the phenylalanine and C-terminal hydrophobic residues. The analysis of the average number of intra- and inter-peptide contacts formed by main-chain atoms per residue revealed a higher number of intra-peptide contacts for residues 4–21 and a lower number of inter-peptide contacts for residues 9–15 (Fig. 5f). This was primarily due to the Y12L substitution, which disrupted the inter-peptide side-chain-side-chain interactions of residue 12 with the aromatic residue abundant region and the C-terminal hydrophobic tail. Future efforts to enhance the amyloid-resistant potential of DM-hCT should concentrate on modifying the mutants of phenylalanine residues and the C-terminal tail hydrophobic residues.

3.6 Double substitutions Y12L and N17H suppressed the β-barrel intermediates.

The discovery of β-barrel oligomers, initially observed in the aggregation of an 11-residue fragment from the heat-shock protein αB-crystalline using X-ray crystallography, raised the possibility that these could be cytotoxic oligomers in amyloidosis[51]. Several prior computational studies have reported the presence of β-barrel intermediates in the aggregation of experimentally determined toxic amyloid peptides[41, 52, 53]. Experimental and computational support for the formation of β-barrel intermediates has also been found in the cases of full-length Aβ[47, 54, 55] and hIAPP[49]. For instance, in wild-type Aβ, a higher propensity for β-barrel formation was observed compared to the AD-protective A2T substitution, but it was lower than in AD-causative mutations of D7N and E22G[47]. Additionally, the substitution of S20G in hIAPP, which exhibited stronger amyloidogenicity and cytotoxicity, resulted in a significant increase in β-barrel formation compared to the wild-type peptide[35]. In line with the hypothesis of toxic β-barrel intermediates, hCT was found to spontaneously nucleate into β-barrel oligomers (Fig. 6). Interestingly, the averaged β-barrel propensity of DM-hCT was significantly lower than that of hCT (Fig. 6a&b). Notably, previous experimental assays have also demonstrated that hCT is much more cytotoxic than DM-hCT[16]. Although the formation of β-barrel intermediates was observed as a rare event in only a few trajectories (Fig. 6b), our findings, indicating a stronger β-barrel propensity in hCT compared to DM-hCT, further support the notion that β-barrels may be the toxic oligomers in amyloidosis. These well-structured 3D β-barrel oligomers (Fig. 6c) could potentially serve as novel therapeutic targets for amyloid-related diseases, such as AD and T2D.

4. Conclusion

In this study, we conducted a series of microsecond-scale atomistic DMD simulations to investigate the folding and self-assembly conformation dynamics of hCT and DM-hCT. Our extensive long-timescale DMD simulations revealed that hCT monomers primarily adopted unstructured conformations, interspersed with dynamic helices around residues 4–21. The Y12L and N17H substitutions increased the stability of this dynamic helix and inhibited the transition towards transient β-sheet conformations, particularly in residues 8–12 of hCT monomers. This observation aligned with prior CD measurements, which showed that DM-hCT exhibited more helical content than hCT in the monomer state[16, 23]. Upon oligomerization, hCT formed β-sheet-rich aggregates and β-barrel intermediates. The

Author Manuscript Author Manuscript Author Manuscript Author Manuscript

β-sheet formation involved residues 8–31, with a notable presence in the phenylalanine-rich region from residues 16–25, consistent with previous NMR measurements[15]. Comparatively, self-assemblies of DM-hCT exhibited an enhancement of helix conformations around residues 4–21 and a reduction in β-sheet formations around residues 8–14. The Y12L substitution disrupted the aromatic interaction of residue 12 with the phenylalanine-rich region, thus preventing β-sheet formation. Furthermore, the increased helical formation around residues 4–21 hindered their participation with the C-terminal hydrophobic tail in β-sheet structures. Notably, the phenylalanine-rich region and C-terminal hydrophobic tail still displayed inter-peptide β-sheets in DM-hCT aggregates. Future amyloid-resistant improvements for DM-hCT should focus on minimizing mutations in phenylalanine and the C-terminal hydrophobic tail to reduce the remaining β-sheets. Interestingly, Y12L and N17H substitutions effectively prevented potential toxic β-barrel formations, and prior cell viability assays indicated a significant reduction in the cytotoxicity of hCT[16]. Our computational results have not only unveiled the molecular mechanisms underlying hCT aggregation and provided insight into the amyloid-resistant effects of Y12L and N17H substitutions in DM-hCT, but have also offered valuable guidance for designing next-generation hCT analogs with clinical applications in mind.

Supplementary Material

Refer to Web version on PubMed Central for supplementary material.

Acknowledgments.

This work was supported in part by the National Natural Science Foundation of China (Grant No. 11904189), Natural Science Foundation of Ningbo (Grant No. 2023J078), Ningbo Top Medical and Health Research Program (Grant No. 2022020304), and US National Institutes of Health R35GM145409. Computer simulations were partially supported by the multi-scale computational modeling core of NIH P20GM121342. The content is solely the responsibility of the authors and does not necessarily represent the official views of the NSFC, NSFN, NIH, and NSF.

References

1. Kamgar-Parsi K, Tolchard J, Habenstein B, Loquet A, Naito A and Ramamoorthy A, Isr J Chem, 2017, 57, 634002D650.
2. Sexton PM, Findlay DM and Martin TJ, Curr Med Chem, 1999, 6, 1067–1093. [PubMed: 10519914]
3. Stenbeck G, Semin Cell Dev Biol, 2002, 13, 285–292. [PubMed: 12243728]
4. Inzerillo AM, Zaidi M and Huang CL, J Pediatr Endocrinol Metab, 2004, 17, 931–940. [PubMed: 15301040]
5. Huang CL, Sun L, Moonga BS and Zaidi M, Cell Mol Biol (Noisy-le-grand), 2006, 52, 33–43.
6. Colman E, Hedin R, Swann J and Orloff D, Lancet, 2002, 359, 885–886. [PubMed: 11897305]
7. Isobe T, Fukasa M and Fujita T, Jpn J Med, 1985, 24, 8–12. [PubMed: 3923241]
8. Silver MM, Hearn SA, Lines LD and Troster M, J Histochem Cytochem, 1988, 36, 1031–1036. [PubMed: 3392392]
9. Ye H, Li H and Gao Z, Nitric Oxide, 2020, 104–105, 11–19.
10. Wada S, Martin TJ and Findlay DM, Endocrinology, 1995, 136, 2611–2621. [PubMed: 7750484]
11. Cudd A, Arvinte T, Das RE, Chinni C and MacIntyre I, J Pharm Sci, 1995, 84, 717–719. [PubMed: 7562410]

Author Manuscript Author Manuscript Author Manuscript Author Manuscript

12. Andreotti G, Vitale RM, Avidan-Shpalter C, Amodeo P, Gazit E and Motta A, J Biol Chem, 2011, 286, 2707–2718. [PubMed: 21078667]
13. Shang H, Zhou A, Jiang J, Liu Y, Xie J, Li S, Chen Y, Zhu X, Tan H and Li J, Acta Biomater, 2018, 78, 178–188. [PubMed: 30076991]
14. Muff R, Dambacher MA and Fischer JA, Osteoporos Int, 1991, 1, 72–75. [PubMed: 1790395]
15. Itoh-Watanabe H, Kamihira-Ishijima M, Javkhlantugs N, Inoue R, Itoh Y, Endo H, Tuzi S, Saito H, Ueda K and Naito A, Phys Chem Chem Phys, 2013, 15, 8890–8901. [PubMed: 23552643]
16. Chen YT, Hu KW, Huang BJ, Lai CH and Tu LH, J Phys Chem B, 2019, 123, 10171–10180. [PubMed: 31692350]
17. Bertolani A, Pizzi A, Pirrie L, Gazzera L, Morra G, Meli M, Colombo G, Genoni A, Cavallo G, Terraneo G and Metrangolo P, Chemistry, 2017, 23, 2051–2058. [PubMed: 27806188]
18. Renawala HK, Chandrababu KB and Topp EM, Biophys J, 2021, 120, 86–100. [PubMed: 33220304]
19. Huang R, Vivekanandan S, Brender JR, Abe Y, Naito A and Ramamoorthy A, J Mol Biol, 2012, 416, 108–120. [PubMed: 22200484]
20. Liu Y, Wang Y, Zhang Y, Zou Y, Wei G, Ding F and Sun Y, J Chem Inf Model, 2023, 63, 308–320. [PubMed: 36456917]
21. Paul S and Paul S, Phys Chem Chem Phys, 2021, 23, 14496–14510. [PubMed: 34184696]
22. Hamid AKM, Salvatore JC, Wang K, Murahari P, Guljas A, Ragyanszki A, Owen M, Jojart B, Szori M, Csizmadia IG, Viskolcz B and Fiser B, Comput Biol Chem, 2019, 80, 259–269. [PubMed: 31048244]
23. Chuang YP, Chang YP and Tu LH, Protein Sci, 2023, 32, e4711. [PubMed: 37354016]
24. Ding F, Tsao D, Nie H and Dokholyan NV, Structure, 2008, 16, 1010–1018. [PubMed: 18611374]
25. Shirvanyants D, Ding F, Tsao D, Ramachandran S and Dokholyan NV, J Phys Chem B, 2012, 116, 8375–8382. [PubMed: 22280505]
26. Proctor EA and Dokholyan NV, Curr Opin Struc Biol, 2016, 37, 9–13.
27. Urbanc B, Borreguero JM, Cruz L and Stanley HE, Methods Enzymol, 2006, 412, 314–338. [PubMed: 17046666]
28. Yin S, Ding F and Dokholyan NV, Nat Methods, 2007, 4, 466–467. [PubMed: 17538626]
29. Yin S, Biedermannova L, Vondrasek J and Dokholyan NV, J Chem Inf Model, 2008, 48, 1656–1662. [PubMed: 18672869]
30. Brodie NI, Popov KI, Petrotchenko EV, Dokholyan NV and Borchers CH, Sci Adv, 2017, 3, e1700479. [PubMed: 28695211]
31. Lazaridis T and Karplus M, Proteins, 1999, 35, 133–152. [PubMed: 10223287]
32. Yanez Orozco IS, Mindlin FA, Ma J, Wang B, Levesque B, Spencer M, Rezaei Adariani S, Hamilton G, Ding F, Bowen ME and Sanabria H, Nat Commun, 2018, 9, 3724. [PubMed: 30214057]
33. Hamilton GL, Saikia N, Basak S, Welcome FS, Wu F, Kubiak J, Zhang C, Hao Y, Seidel CAM, Ding F, Sanabria H and Bowen ME, Elife, 2022, 11, e77242. [PubMed: 36069777]
34. Liu Y, Wang Y, Tong C, Wei G, Ding F and Sun Y, Small, 2022, 18, e2202642. [PubMed: 35901284]
35. Wang Y, Liu Y, Zhang Y, Wei G, Ding F and Sun Y, Phys Chem Chem Phys, 2022, 24, 21773–21785. [PubMed: 36098068]
36. Kabsch W and Sander C, Biopolymers, 1983, 22, 2577–2637. [PubMed: 6667333]
37. Huang F, Wang Y, Zhang Y, Wang C, Lian J, Ding F and Sun Y, J Chem Inf Model, 2023, 63, 3591–3600. [PubMed: 37253119]
38. Wang Y, Xu J, Huang F, Yan J, Fan X, Zou Y, Wang C, Ding F and Sun Y, J Chem Inf Model, 2023, 63, 3567–3578. [PubMed: 37246935]
39. Daura X, Gademann K, Jaun B, Seebach D, van Gunsteren WF and Mark AE, Angew Chem Int Edit, 1999, 38, 236–240.
40. Zhang Y, Wang Y, Liu Y, Wei G, Ding F and Sun Y, ACS Chem Neurosci, 2022, 13, 3126–3137. [PubMed: 36278939]

Author Manuscript Author Manuscript Author Manuscript Author Manuscript

41. Sun Y, Huang J, Duan X and Ding F, J Chem Inf Model, 2021, 61, 966–975. [PubMed: 33445870]
42. Amodeo P, Motta A, Strazzullo G and Castiglione Morelli MA, J Biomol NMR, 1999, 13, 161–174. [PubMed: 10070757]
43. Kamihira M, Naito A, Tuzi S, Nosaka AY and Saito H, Protein Sci, 2000, 9, 867–877. [PubMed: 10850796]
44. Swindells MB, MacArthur MW and Thornton JM, Nat Struct Biol, 1995, 2, 596–603. [PubMed: 7664128]
45. Munoz V and Serrano L, Proteins, 1994, 20, 301–311. [PubMed: 7731949]
46. Kanaori K and Nosaka AY, Biochemistry, 1995, 34, 12138–12143. [PubMed: 7547953]
47. Sun Y, Kakinen A, Wan X, Moriarty N, Hunt CPJ, Li Y, Andrikopoulos N, Nandakumar A, Davis TP, Parish CL, Song Y, Ke PC and Ding F, Nano Today, 2021, 38, 101125. [PubMed: 33936250]
48. Nguyen PH and Derreumaux P, J Chem Phys, 2023, 158, 235101. [PubMed: 37318171]
49. Sun Y, Kakinen A, Xing Y, Pilkington EH, Davis TP, Ke PC and Ding F, Biochim Biophys Acta Mol Basis Dis, 2019, 1865, 434–444. [PubMed: 30502402]
50. Guo AZ, Fluitt AM and de Pablo JJ, J Chem Phys, 2018, 149, 025101. [PubMed: 30007378]
51. Laganowsky A, Liu C, Sawaya MR, Whitelegge JP, Park J, Zhao M, Pensalfini A, Soriaga AB, Landau M, Teng PK, Cascio D, Glabe C and Eisenberg D, Science, 2012, 335, 1228–1231. [PubMed: 22403391]
52. Sun Y, Ge X, Xing Y, Wang B and Ding F, Sci Rep, 2018, 8, 10353. [PubMed: 29985420]
53. Do TD, LaPointe NE, Nelson R, Krotee P, Hayden EY, Ulrich B, Quan S, Feinstein SC, Teplow DB, Eisenberg D, Shea JE and Bowers MT, J Am Chem Soc, 2016, 138, 549–557. [PubMed: 26700445]
54. Wu J, Blum TB, Farrell DP, DiMaio F, Abrahams JP and Luo J, Angew Chem Int Ed Engl, 2021, 60, 18680–18687. [PubMed: 34042235]
55. Osterlund N, Moons R, Ilag LL, Sobott F and Graslund A, J Am Chem Soc, 2019, 141, 10440–10450. [PubMed: 31141355]

Author Manuscript Author Manuscript Author Manuscript Author Manuscript

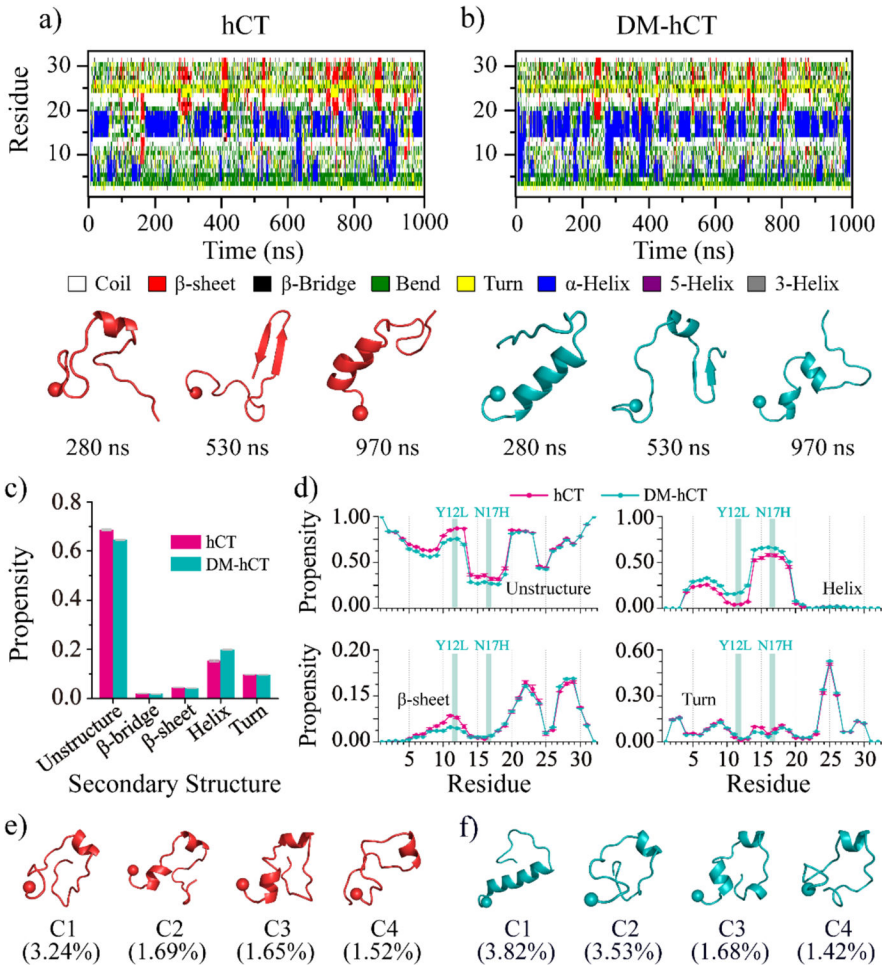

Fig. 1. Conformational dynamics of hCT and DM-hCT monomers.

The time evolution of the secondary structure of each residue within hCT **a)** and DM-hCT **b)** monomers is depicted. Three snapshots with corresponding time stamps are provided below to illustrate transient conformations. For each molecular system, one trajectory is randomly selected from fifty independent simulations to illustrate the conformational dynamics. The average secondary structure contents of unstructured (coil and bend), β-sheet, helix, and turn conformations for hCT and DM-hCT during the last 500 ns from fifty independent 1000 ns DMD simulations are shown in **c)**. The average propensity of each residue from hCT and DM-hCT monomers adopting unstructured, helix, β-sheet, and turn conformations is displayed in **d)**. Representative conformations of the top 4 most-populated clusters of hCT **e)** and DM-hCT **f)** with the N-terminal Cα atom highlighted as a bead. For clarity, hCT and DM-hCT are colored red and cyan, respectively.

Author Manuscript Author Manuscript Author Manuscript Author Manuscript

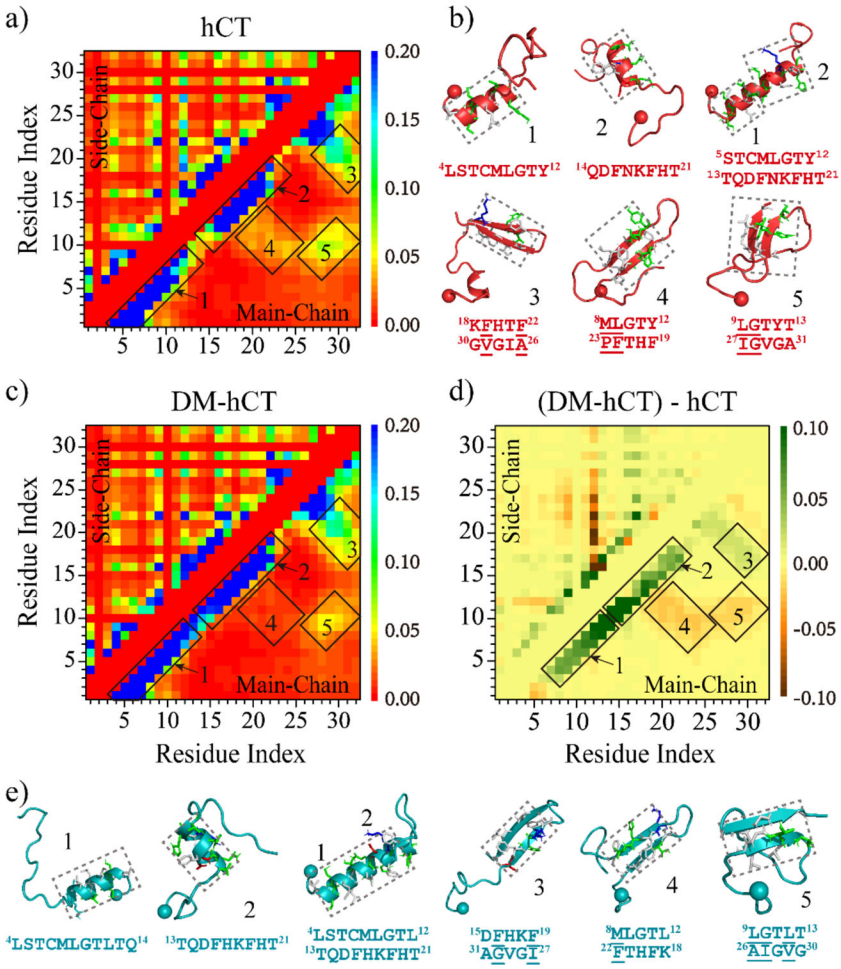

Fig. 2. Residue-pairwise contact frequency analysis for hCT and DM-hCT monomers.

The residue-pairwise contact frequency of the hCT monomer is shown in **a)**. Representative structured contact patterns are labeled as 1–5, corresponding to the structures presented in **b)**. The residue-pairwise contact frequency of the DM-hCT monomer is displayed in **c)**, and its corresponding difference from hCT is shown in **d)**. The difference is calculated by subtracting the corresponding residue-pairwise contact propensity of hCT from DM-hCT. The same structured contact patterns region of hCT is also correspondingly labeled in **c)** and **d)** for DM-hCT, with the corresponding structures shown in **e)**. The analysis is based on the data of the last 500 ns from 1000 ns simulations conducted in fifty independent runs for each molecular system. For clarity, hCT and DM-hCT are colored red and cyan, respectively, with the N-terminal Cα atom labeled as a bead.

Author Manuscript Author Manuscript Author Manuscript Author Manuscript

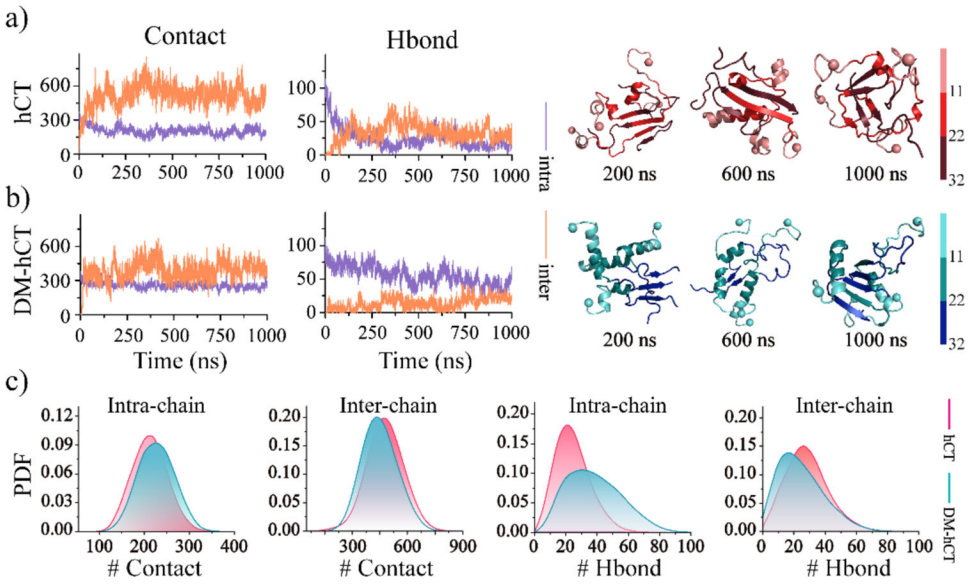

Fig. 3. Oligomerization dynamics analysis of four peptides of hCT and DM-hCT.

The number of backbone hydrogen bonds and heavy contacts is presented as a function of simulation time in the four-peptide simulation of hCT **a)** and DM-hCT **b)**. Corresponding snapshots at 200, 600, and 1000 ns are shown on the right. One out of fifty independent trajectories is randomly selected to illustrate the self-assembly dynamics. Probability distributions for the number of intra- and inter-peptide heavy-atom contacts (left) and hydrogen backbone bonds (right) in the saturated self-assemblies of hCT and DM-hCT are displayed in **c)**. The saturated hCT and DM-hCT self-assemblies correspond to the conformations of the last 500 ns from 1000 ns DMD runs in fifty independent trajectories. For clarity, each peptide within the hCT and DM-hCT self-assemblies is color-coded from light to dark in red and cyan, respectively. The N-terminal Cα atom of each peptide is indicated as a bead.

Author Manuscript Author Manuscript Author Manuscript Author Manuscript

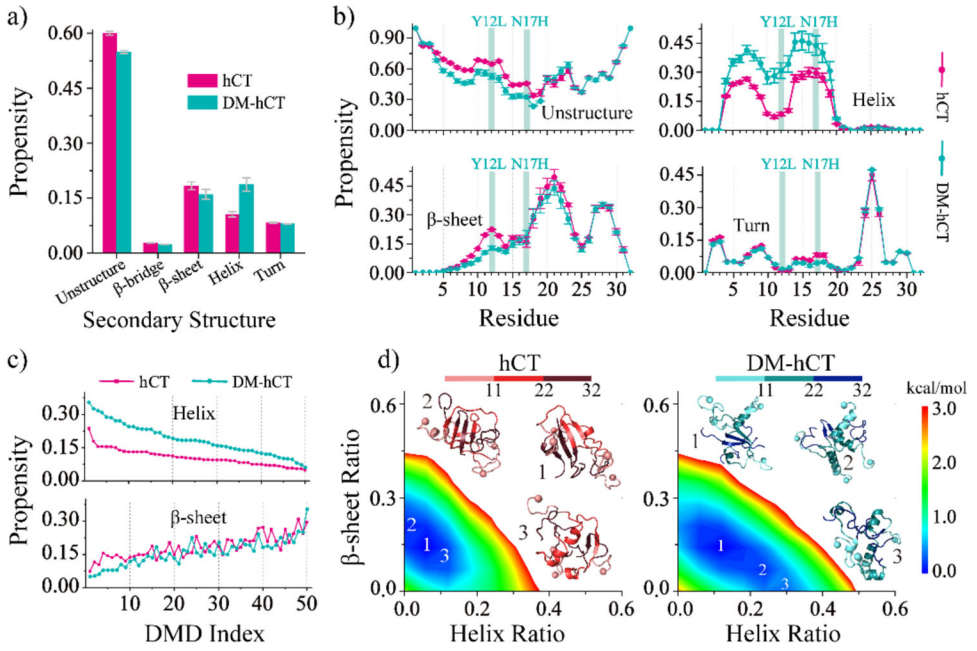

Fig. 4. Secondary structure analysis of the self-assemblies of hCT and DM-hCT.

The average content of each secondary structure in the self-aggregates of hCT and DM-hCT **a)**. The average propensity of each residue from hCT and DM-hCT, assuming unstructured, helix, β-sheet, and turn conformations in their corresponding aggregates **b)**. The error bars of secondary structure propensities correspond to the standard deviations of means from fifty independent simulations. The average helix (top) and β-sheet (bottom) probability of each independent four-peptide hCT and DM-hCT simulation, with the trajectory index sorted by the helical content from high to low **c)**. The conformational free energy landscape as a function of the helix and β-sheet ratio of each aggregate formed by hCT (left panel) and DM-hCT (right panel) **d)**. Three representative snapshots with the helix and β-sheet contents corresponding to the deepest basin region are randomly selected for illustration as insets. Only the last 500 ns data out of 1000 ns from fifty independent DMD trajectories are used for the above secondary structure analysis. For clarity, each peptide within the hCT and DM-hCT self-assemblies is color-coded from light to dark in red and cyan, respectively. The N-terminal Cα atom is highlighted as a bead.

Author Manuscript Author Manuscript Author Manuscript Author Manuscript

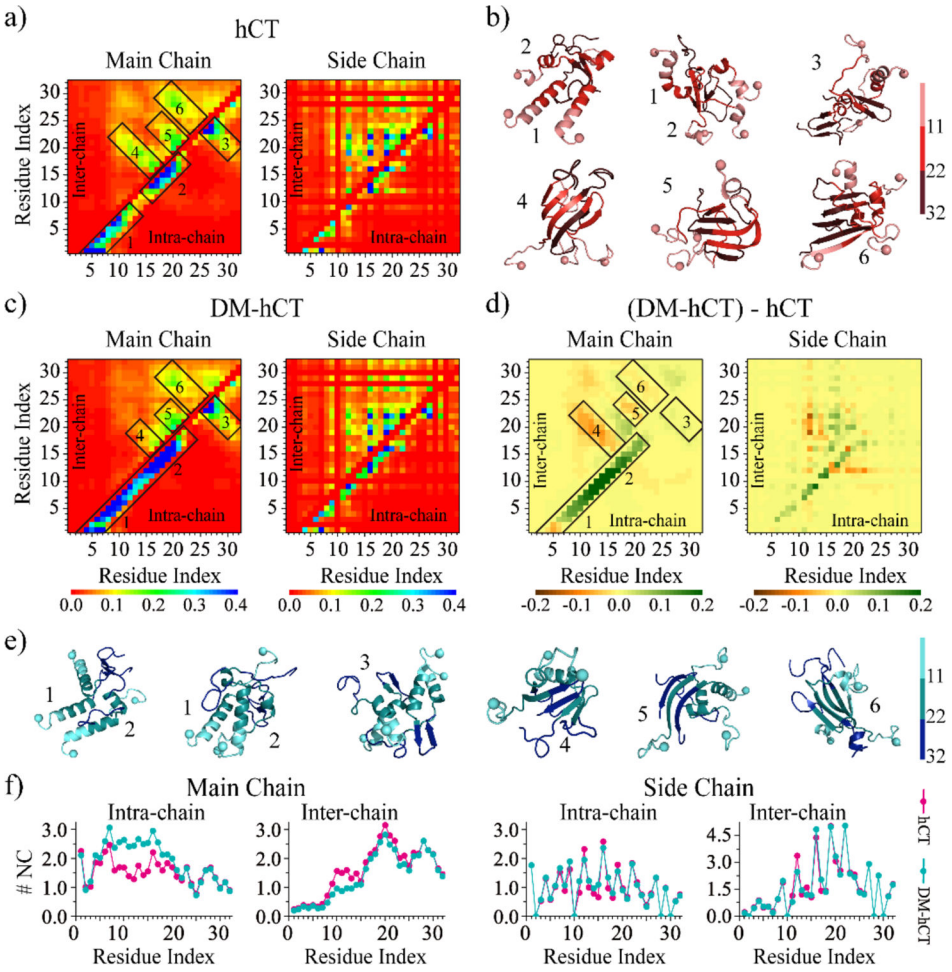

Fig. 5. Interactions among residues driving the self-assembly of hCT and DM-hCT.

Intra-chain (lower diagonal) and inter-chain (upper diagonal) residue-pairwise contact frequencies of main-chain (left column) and side-chain (right column) atoms for the aggregates of hCT **a)** and DM-hCT **c)**. The representative structured contact patterns with a high average contact frequency are labeled as 1–6, and the corresponding structures highlighted by boxes in the contact frequency map are also presented in **b)** and **e)**. For each system, six representative aggregated structures are selected based on contact frequency. The residue-pairwise contact frequency differences of DM-hCT with respect to wild-type hCT are calculated by subtracting each corresponding residue-pairwise contact propensity of hCT from the DM-hCT **d)**. The average number of inter- and intra-peptide contacts per residue formed by atoms from the main-chain and side-chain are also computed for hCT and DM-hCT **f)**. For clarity, each peptide within the hCT and DM-hCT self-assemblies is color-coded from light to dark in red and cyan, respectively, with the N-terminal Cα atom of each peptide indicated as a bead.

Author Manuscript Author Manuscript Author Manuscript Author Manuscript

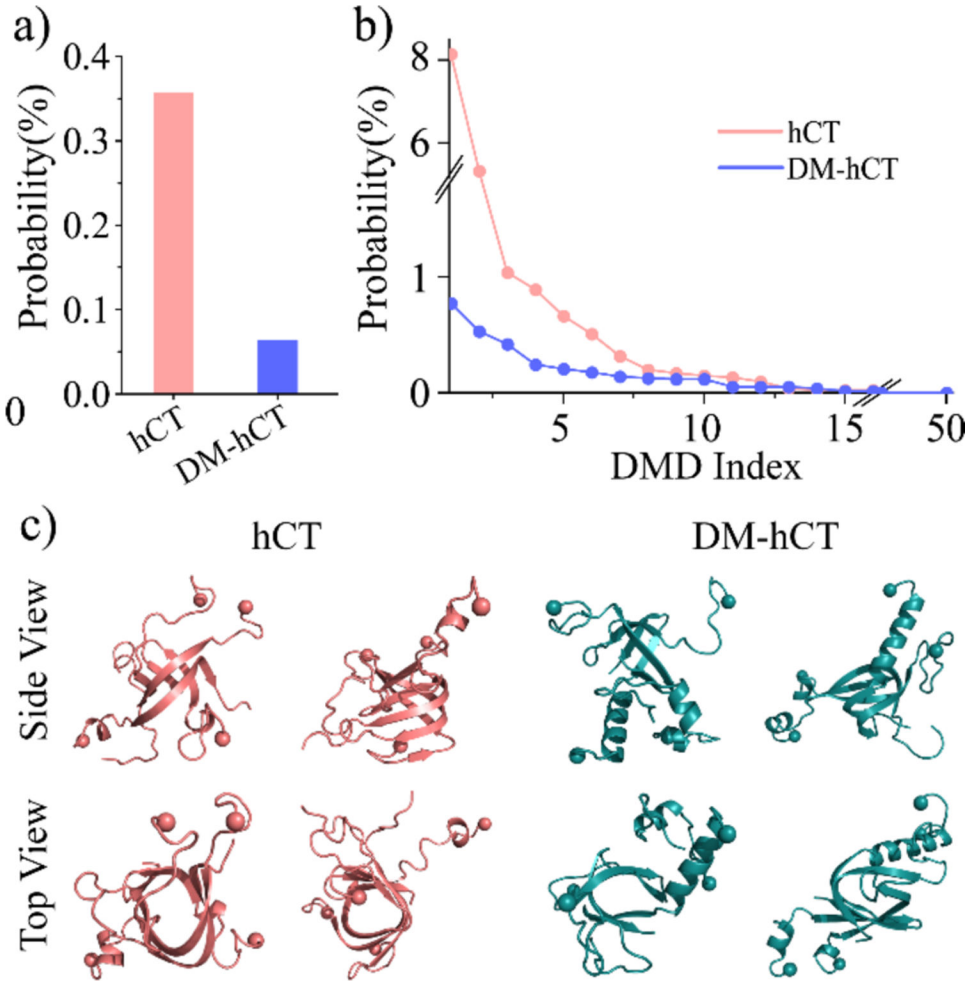

Fig. 6. The β-barrel conformation analysis for hCT and DM-hCT.

The average probability of β-barrel oligomers observed in the fifty independent DMD trajectories for hCT and DM-hCT **a)**. Two representative β-barrel structures formed by hCT and DM-hCT are presented in two different views (side and top) **b)**. Due to the highly heterogeneous structure of β-barrels, two representative β-barrels are randomly selected from the top-most populated β-barrel trajectories.

Author Manuscript

Author Manuscript

Author Manuscript

Author Manuscript

Table 1.

The amino acid sequences of hCT and DM-hCT both include a C1–C7 intra-peptide disulfide bond. For clarity, hydrophobic, hydrophilic, negatively charged, and positively charged residues are color-coded in black, green, red, and blue, respectively.

	squence
	S-S 10 20 30
hCT	CGNLSTCMLG TYTQDFNKFH TFPQTAIGVG AP
DM-hCT	CGNLSTCMLG TLTQDFHKFH TFPQTAIGVG AP

Author Manuscript

Author Manuscript

Author Manuscript

Author Manuscript

Table 2.

The details of each molecular system simulation, including the number of simulated peptides (system), the type of calcitonin peptide (peptide), cubic simulation box dimensions (box size), the number of independently performed DMD simulations for each molecular system (DMD run), the duration time of each independent DMD simulation (time), and the cumulative total simulation time.

system	peptide	box size (nm)	DMD run	time (μs)	total time (μs)
1-peptide	hCT	6.5	50	1	50
	DM-hCT	6.5	50	1	50
4-peptides	hCT	9.5	50	1	50
	DM-hCT	9.5	50	1	50